Supplementary information

3D printing stretchable and compressible porous structures by polymerizable emulsions for soft robotics

Ouriel Bliah, Seonggun Joe, Roei Reinberg, Anderson B. Nardin, Lucia Beccai and Shlomo Magdassi

This supporting information includes:

Section 1: Comparison table of the developed emulsion relative to the state of the art.

Table S1: Comparison table of 3D-DLP printable materials based on emulsion templating.

Type	Materials*	Material Behavior	Discussed Application	Ref
O/W emulsion	DPHA, TMPTA, DPGDA	Brittle	Conductive objects by embedding silver NPs	1
W/O HIPEs	DMDD, GMA, PEGDA	-	Biodegradable Porous Polymer	2
O/W HIPEs	HDDA	Brittle	Gas filters	3
O/W emulsion	GelMA, GGMMA	Flexible, Max strain – 50%	Biological cell scaffold	4
W/O HIPE	TMPTA	Brittle	-	5
W/O HIPE	2-ethylhexyl-acrylate, IBOA,TMPTA	Brittle	Biological cell scaffold	6
W/O HIPE	HDDA, TEMPIC	Brittle	Biological cell scaffold	7
This work	Stretchable PUA	Highly stretchable and compressible	Soft robotics, impact resistance, stretchable sensors	-

*dipentaerythritol hexaacrylate (DPHA), trimethylolpropanetriacrylate (TMPTA) and dipropylenglycol diacrylate (DPGDA), poly(ethylene glycol) diacrylate (PEGDA) glycidyl methacrylate (GMA) 3,6-Dimethyl-1,4-dioxane-2,5-dione (DMDD), methacrylated gelatin (GelMA), methacrylated galactoglucomannan(GGMMA),Isobronyl acrylate (IBOA),polyurethane acrylate (PUA), 1,6-hexanediol diacrylate (HDDA), tris 2-(3-mercaptopropionyloxy)ethyl isocyanurate (TEMPIC),polyurethane diacrylate (PUA)

Section 2: Emulsion Development and Stability.

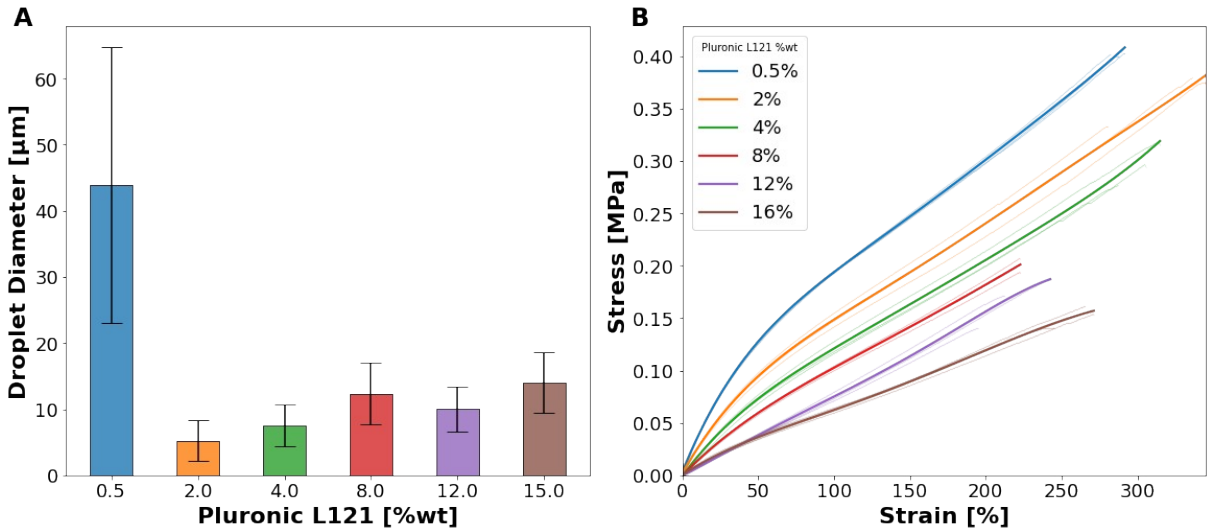

Supplementary Fig. S1: A. Average diameter of droplets at various concentrations of PL121 B. Regression plot based on sets of three tensile tests of different surfactant concentrations

Instability measurements were performed on emulsion containing 35 %wt using LUMifuge analytical centrifuge, it was found that the instability index of the emulsion remained low (no phase separation) even after 9 hours, which corresponds to ~49 hours (measurement performed at 4000 rpm, under 5.54 g). Therefore it can be concluded that for half of the time, 24 hours, the emulsion is completely stable.

To validate these results, mechanical tests were performed on emulsions that were 3D printed and post-treated immediately after preparation, and 24 hours later. These tests showed that the mechanical properties remain unchanged, indicating that the stability of the emulsion does not degrade the quality of the resulting printed parts in this timeframe.

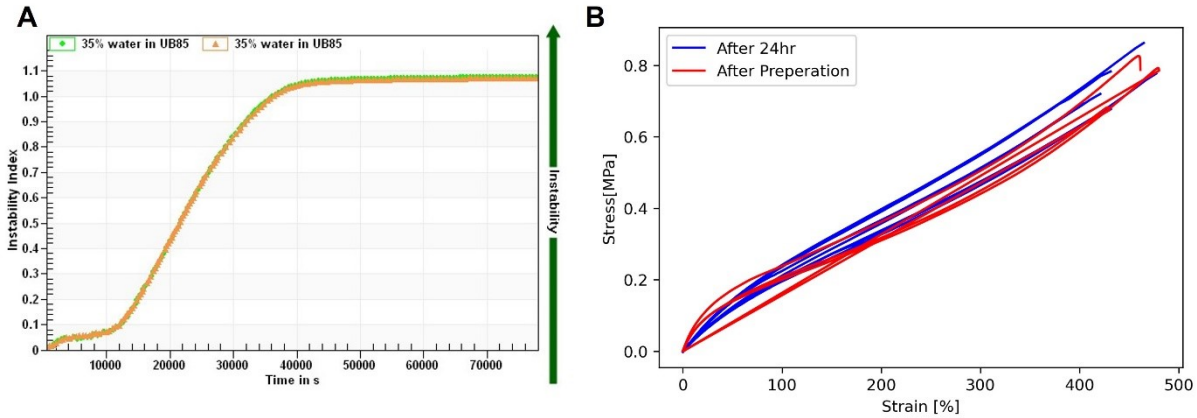

Supplementary Fig. S2: A.Instability measuerment over time for emulsion containing 35% wt water,the measurment was taken at 5.54 time earth acceleration-g. B.Tensile test of on emulsions that were 3D printed and post-treated immediately after preparation and after 24 hours

Section 3: SEM images of the polymerized emulsion at the cross-section focused on holes to show the interconnectivity of the pores.

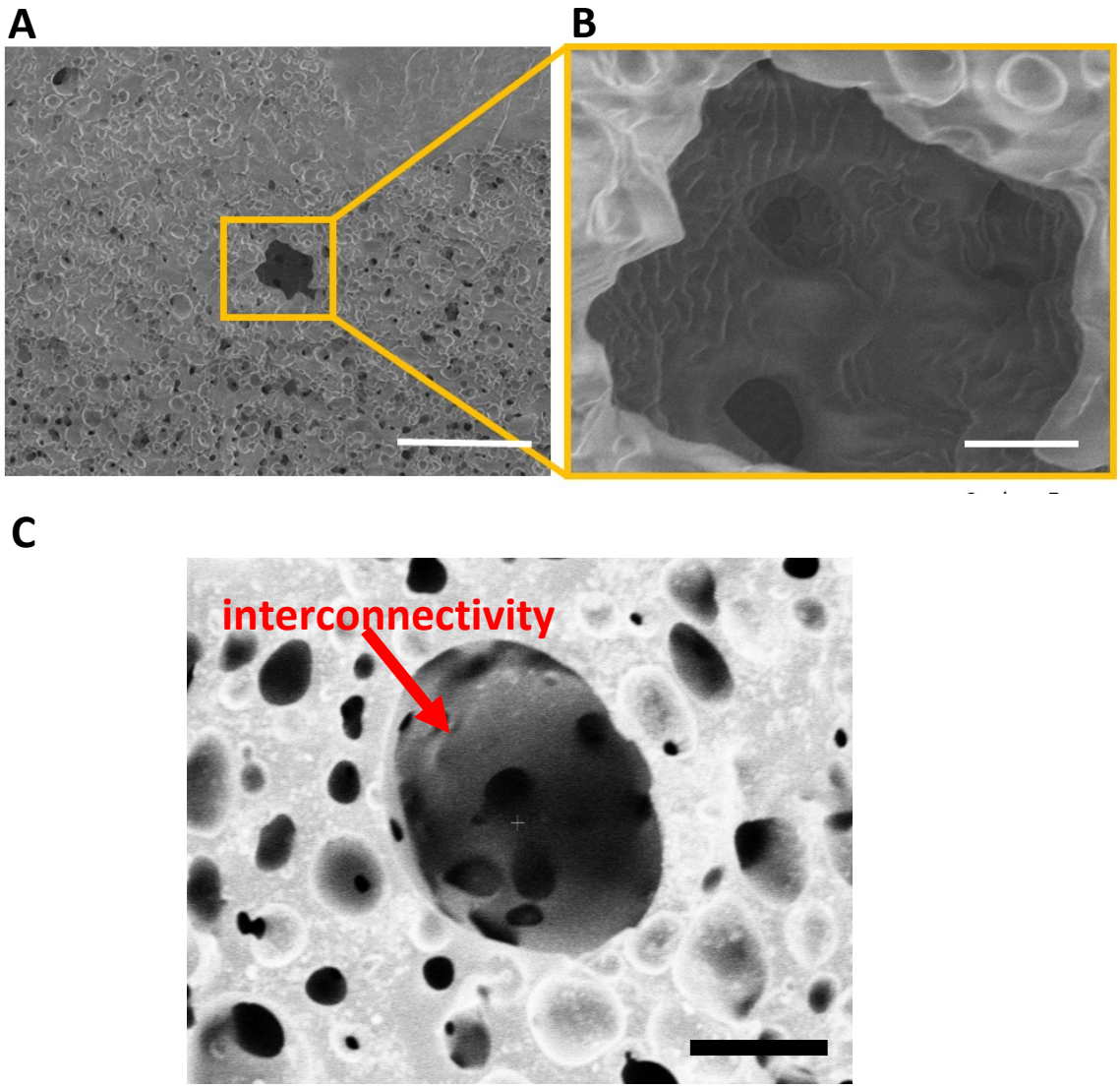

Supplementary Fig. S3: SEM images of the polymerized emulsion Cross section at 35 %wt water focused on holes to show the interconnectivity of the pores. A scale bar=50 µm.B. scale bar=5 µm. C. scale bar=25 µm

Section 4: SEM images of polymerized emulsion with different water concentrations.

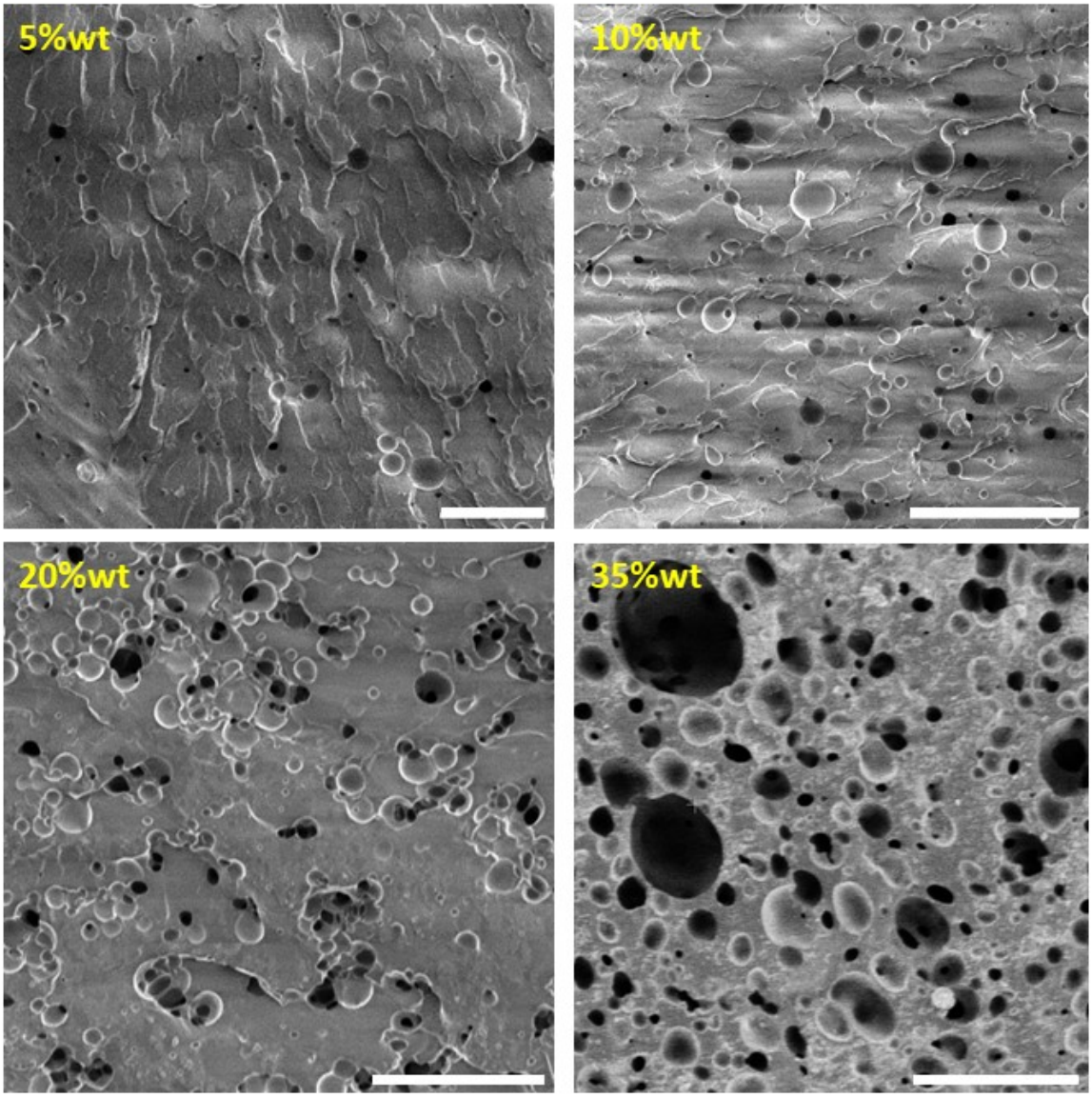

Supplementary Fig. S4: SEM images of polymerized emulsion with different water concentration (%wt) scale bar = 50µm. A. 5%wt B. 10 %wt C. 20 %wt D. 35 %wt

Section 5: Reversible compressibility evaluations at 80% and 20% of emulsion containing 0-35 %wt water

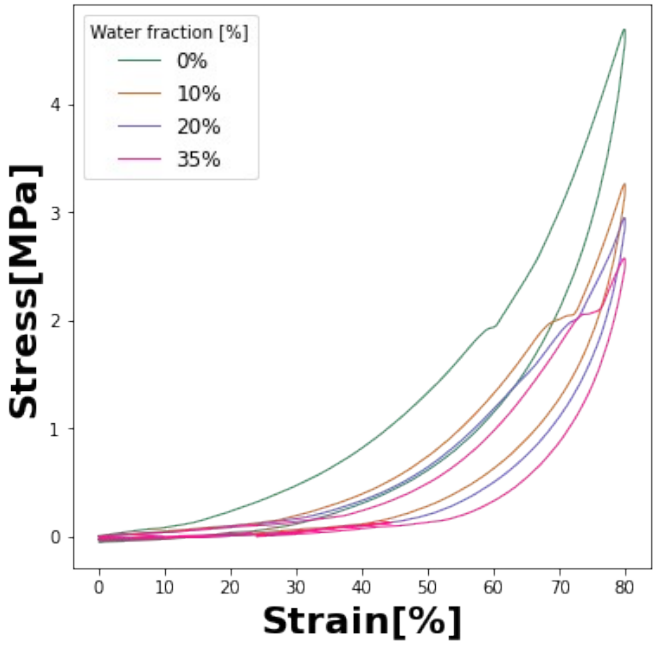

Supplementary Fig. S5: Full cycle of an 80% load-release compressibility measurement of different printable emulsions with varying water fraction.

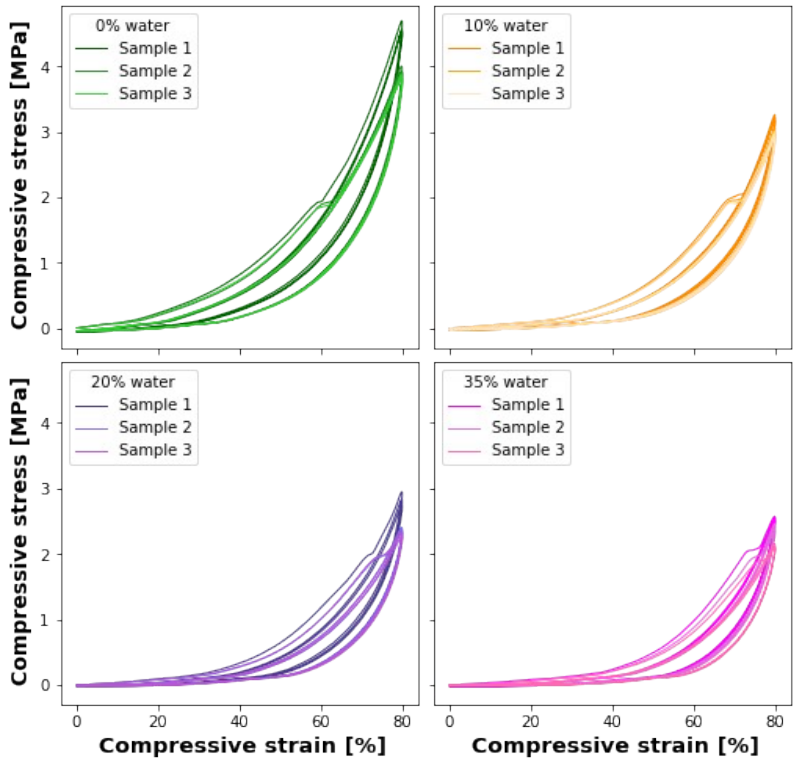

Supplementary Fig S6: Reversible compressability test at 80% compression for emulsion containing 0, 10, 20 and 35 %wt water (upper left to lower right respectively)

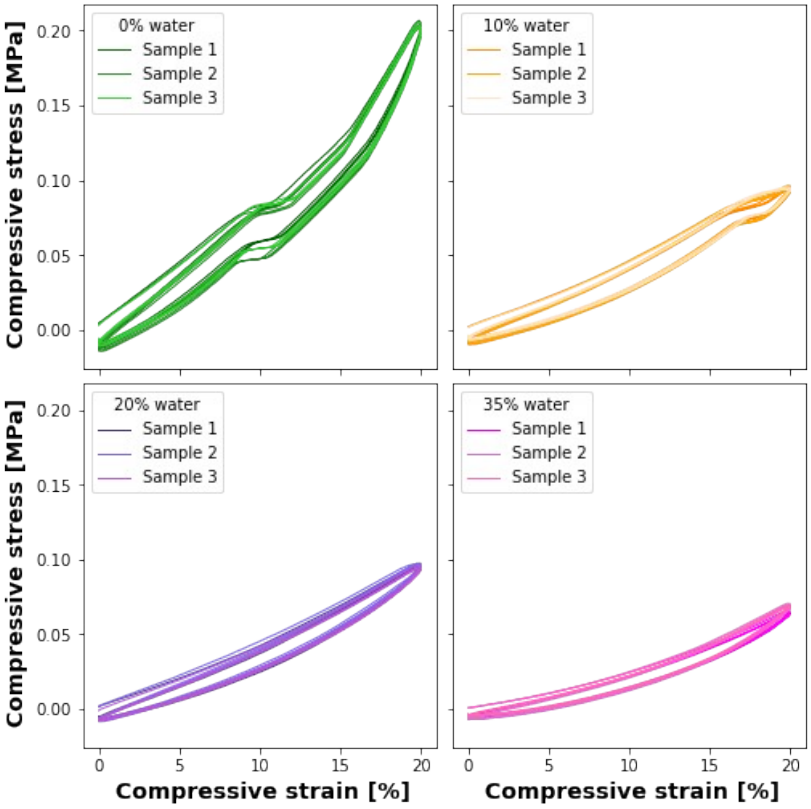

Supplementary Fig S7. Reversible compressability test at 20% compression for emulsion containing 0,10,20,35 %wt water (upper left to lower right respectively)

Section 6: Setup for adhesion force evaluation

The development of 3D printing process requires matching the printing compositions to the printing technology. For the DLP printing, the most important factors are the ink viscosity and stability, polymerization time, and compatibility with the printer components. The last requirement is related to obtaining, on the one hand, adhesion to the printing platform and, on the other hand, avoiding sticking to the vat window, which is composed of transparent FEP film (fluorinated ethylene propylene). When the first layer of the emulsion ink is polymerized on the printing platform, the adhesion of the layer fails due to the presence of water droplets, thus causing the built structures to fall from the platform. This problem was solved by first printing a 300 μm layer of PUA only, thus providing a layer that could adhere better to the continuous phase of the emulsion since both are composed of the same polymer.

The second problem was that the emulsion adhered to the vat window after printing. This is a common problem, which so far has been addressed with several approaches, such as modifying the vat film to reduce its surface energy, by using special membranes as reported for in Continuous Liquid Interface Production(CLIP)[8] or by using hydrogel surfaces[9]. Although these methods can be successful, they require very complicated and precise preparation processes. Our new approach is based on reducing the adhesion between the printing composition, simply by adding a silicone-based surfactant (modified polyether-polysiloxane,ABIL90) to the ink. However, since the additional surfactant may affect the emulsion stability, we tested the stability with an analytical centrifuge (LUMIfuge). The measurement was performed on emulsions without ABIL90 and with ABIL90 at 1 and 2 %wt (Supplementary Fig. S8). As shown, the instability index did not change significantly between the emulsions with and without the added surfactant therefore, ABIL90 did not affect the emulsion stability.

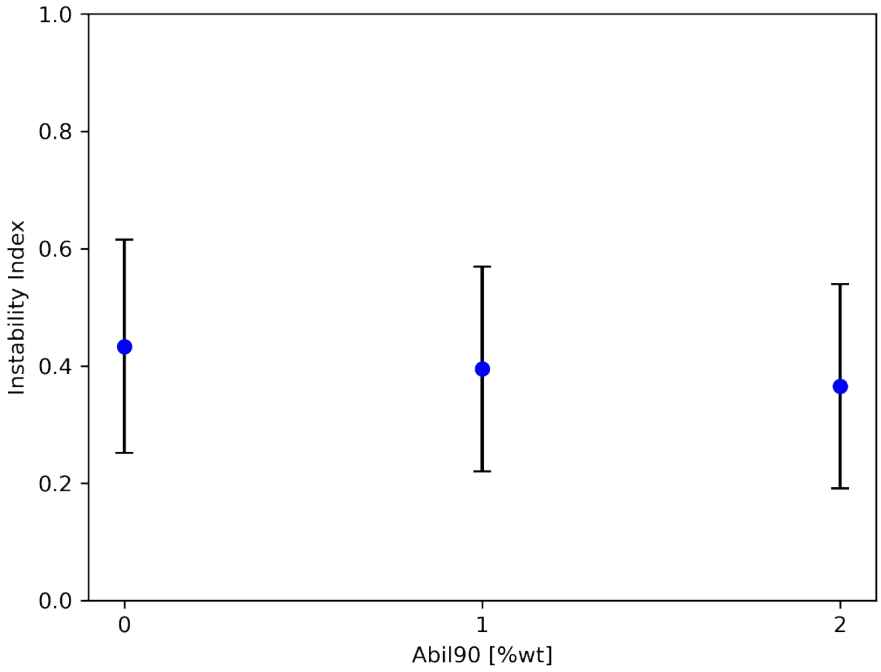

Supplementary Fig. S8. Instability index by analytical centrefuge of the emulsion with varing concentration of ABIL90 surfactant

A quantitative evaluation of the adhesion force of the polymerized emulsion to the FEB film, in presence of the surfactant, was performed by measuring the force required to detach the polymerized layer from the FEB surface. The measurements were performed by an experimental setup that simulates the process of a single-layer printing, with the exact printing conditions of the 3D printer and with the same FEB film (schematically shown in Supplementary Fig. S9A and Fig. S10). For this, the downward movement of the platform and the layer formation were performed within the 3D printer, and the upward movement was done by the force measurement instrument. The force required to detach the polymerized layer from the film, as a function of surfactant concentration, is presented in Supplementary Fig. S9B. As seen, the force decreases from 12 N to 4 N, with the increase of surfactant concentration from 0 to 1 %wt, and remains about the same at higher surfactant concentrations. By printing experiments, it was found that 4N was sufficient to enable layer detachment while printing. Overall, there were no film adhesion issues at surfactant concentrations above 1%.

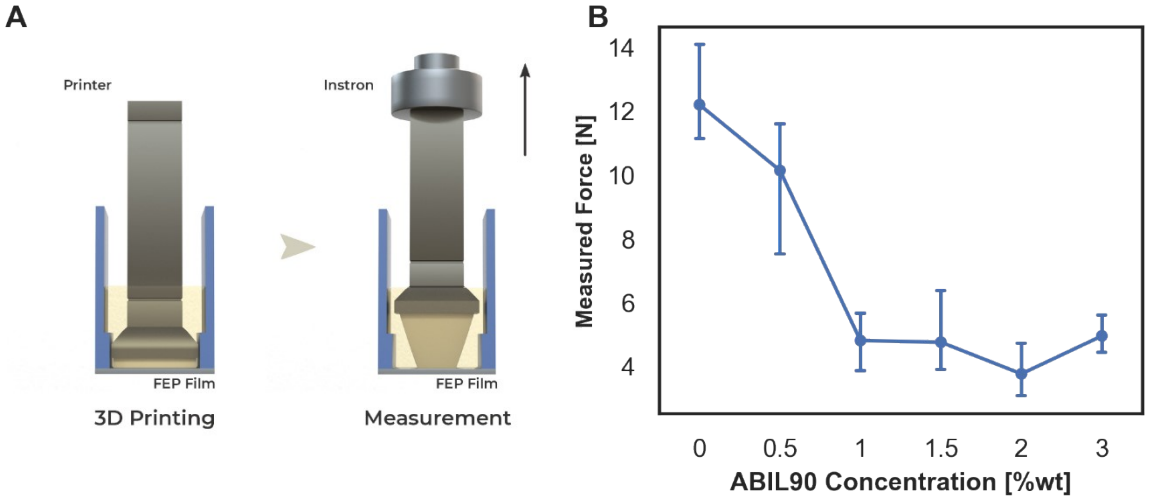

Supplementary Fig S9. A. Schematic presentation of the self-designed force measurement setup. B. Force measured for layer detachment from the FEP film at various concentrations of 0-3%.

Measurment setup: we designed a setup that simulated the process of a single-layer printing where the descending of the platform and layer formation will be done by the printer, and the upraising will be done by the force measurement instrument. As schematically shown in Supplementary Fig. S10, the setup is comprised of the following parts: The vat, which is composed of two parts, the vat base(Supplementary Fig. S10A), where the FEB film is placed, and the vat locker (Supplementary Fig. S10B), that is placed on the vat base securing and stretching the FEB film. The vat base locker is also designed to fit in the adapter for the Instron lower plate (Supplementary Fig. S10C). To print a layer, the printer head(Supplementary Fig 10-D) and the printer adapter (Supplementary Fig. S10E) are connected when the printer movement is downward, and after the layer is formed, the printer head is detached from the adapter. The full setup is schematically shown in Supplementary Fig. S10F.

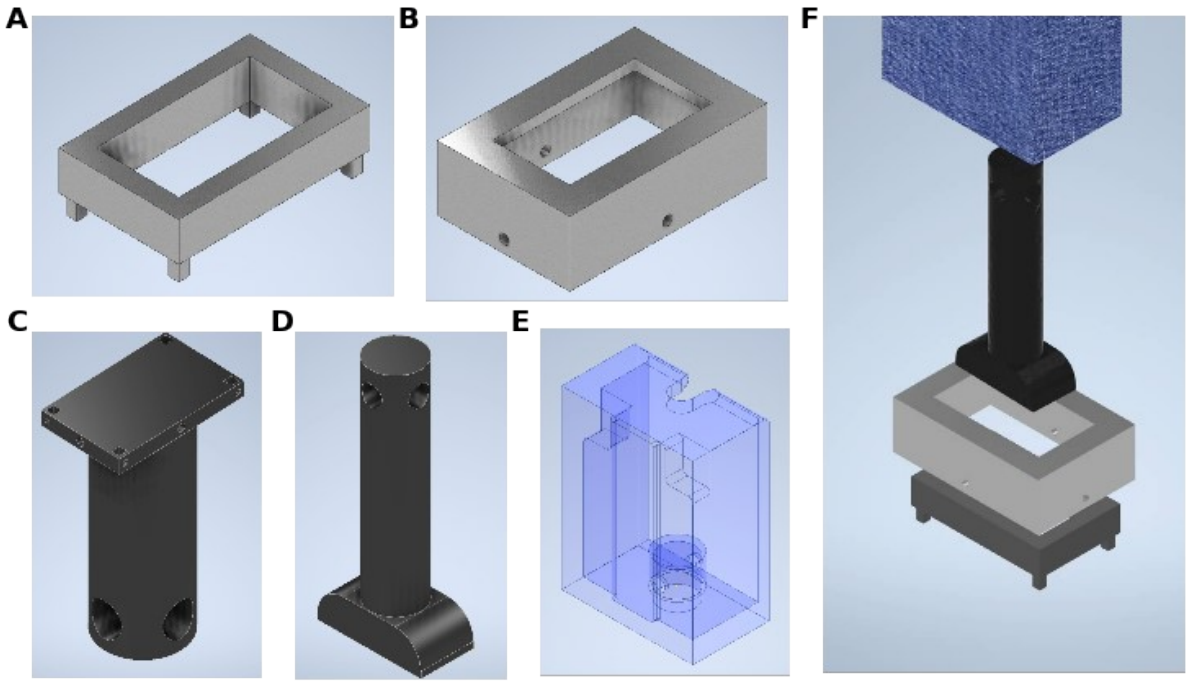

Supplementary Fig. S10: Setup for adhesion to FEB film measurement. A.Vat base B. Vat locker C. Adapter to Instron. D. Printer head E. DLP printer adapter F. Schematic illustration of the full setup

In Supplementary Fig. **S**11 actual images of the setup and operation are presented. As described above, in the first step, the printed performs the downward movement (Supplementary Fig S11A), and when reaching the bottom, a single layer is created. Then the printer head and the adapter are disconnected (Supplementary Fig. S11B). Then, the system is carfully placed to the instron where the vat is connected by the adapter to the instron lower plate and the printer head is designed to fit in the Instron loading cell(Supplementary Fig. S11C). Finally, after securing the setup the Instron performs the upward movement, detaching the printed layer from the FEB film while measuring the force.

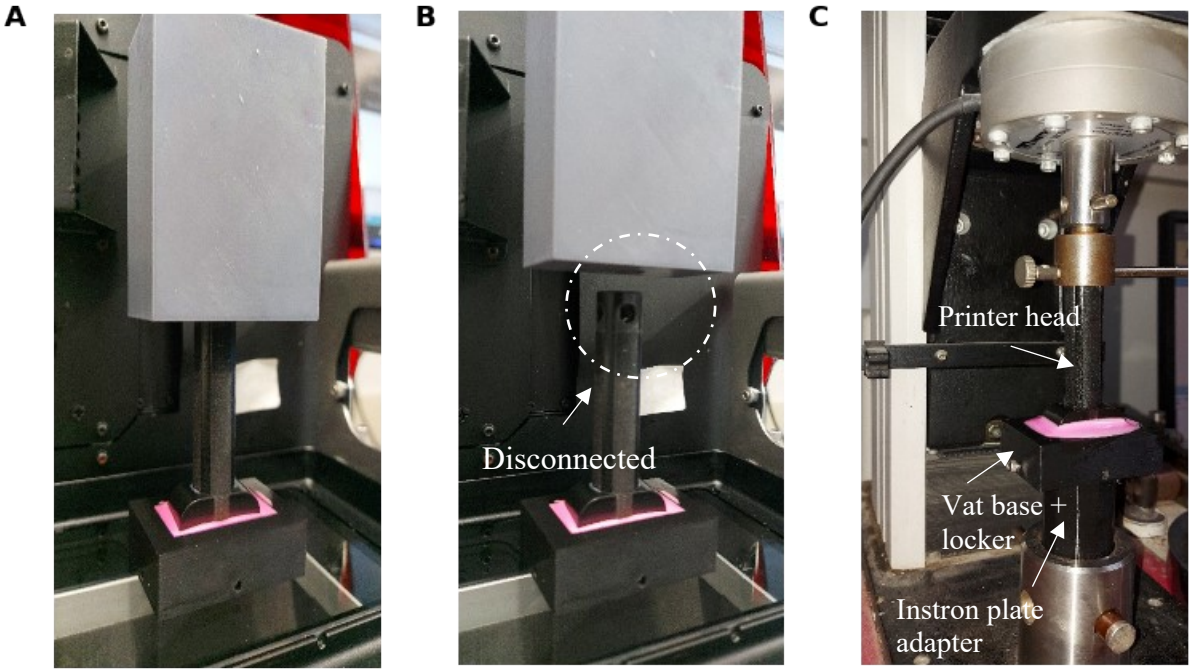

Supplementary Fig. S11: Pictures of the adhesion force setup measurement operation. A. the first step, the printing pf the layer. B. the detachment of the printer adapter and the printer head. D. connection to the Instron force instrument

Section 7: ATR-FTIR measurements and DOC calculation

The degree of conversion during irradiation was determined by following the disappearance of the acrylate double bond relative to the constant carbonyl group by ATR-FTIR measurements, as presented in Supplementary Fig. S13. The conversion value was calculated as:

$$DOC = \frac{\left(\frac{C_{C-H}}{C_{C=O}}\right)_{t=0} - \left(\frac{C_{C-H}}{C_{C=O}}\right)_{t}}{\left(\frac{C_{C-H}}{C_{C=O}}\right)_{t=0}} * 100\%$$

Where C-H is the acrylate peak at 808 cm^{-1} (Supplementary Fig. 8: green area) and C=O stretching is the carbonyl group at 1720 cm^{-1}. [10] To validate the results, the measurement was performed by following the acrylate C=C stretching at 1407 cm^{-1} (Supplementary Fig. S12: yellow area) relative to the same C=O stretching as well.

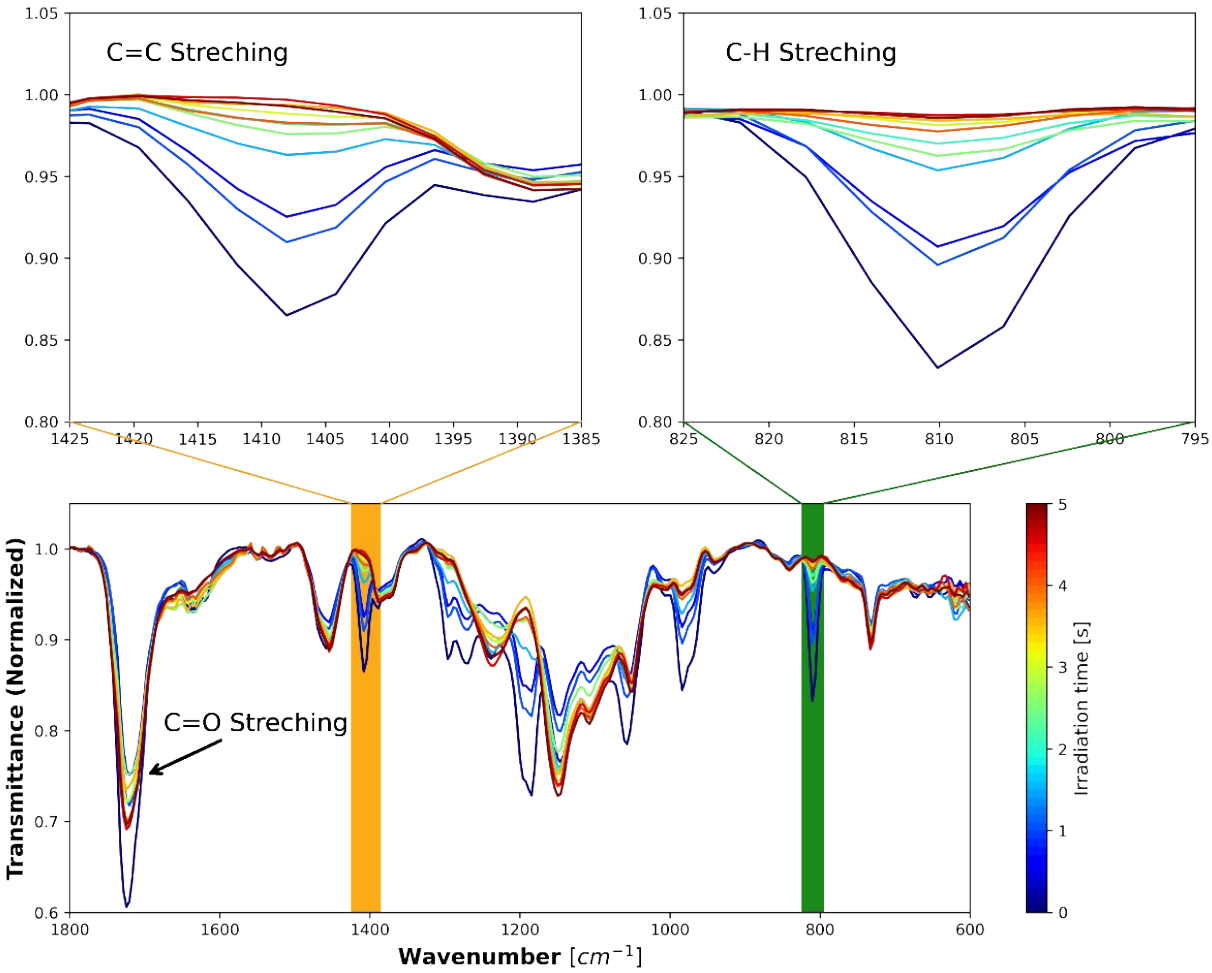

Supplementary Fig. S12: ATR-FTIR measurement of C-H and C=C stretching of the acrylate compared to carbonyl C=O stretching at different exposure time.

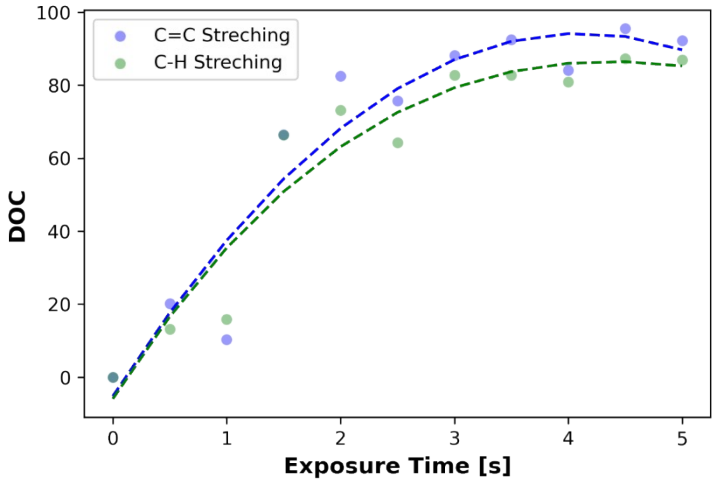

Supplementary Fig. S13: Double bond conversion (DOC) as a function of exposure time.

Section 8: Polymerized emultion(35%wt) air tightness test

To assess the air tightness of the system, a pneumatic line was designed. The line incorporates a 3-way valve that enables the closure of the line where only the actuator remains, ensuring that any air leakage comes solely from the balloon. As depicted in Fig. S14A, the pneumatic line comprises a compressor that connects to an air tank regulating the air oscillation and providing a stable pressure. To control the pressure, a pressure regulator is utilized, and the closed system is linked to the actuator and pressure sensor through a valve. Furthermore, the pressure sensor (KITA-KP25C) is connected to an arduino device through the analog output. A signal calibration is conducted by setting a known pressure through the regulator, allowing for the extrapolation of the exact pressure within our working pressure range (Fig. S14B).

The air tightness test was conducted on a 3D printed balloon composed of an emulsion containing 35%wt water. A pressure of 12 kPa was applied (Fig. S14C), followed by the valve's closure. The pressure remained unchanged for over 10 minutes, as depicted in Fig. S14D. This indicates that while the inner-open pore structure has the potential to impact air tightness and consequently affect the application of pneumatic soft robots, the air leakage is minor. Therefore, based on the results of the air tightness test, it can be concluded that a pneumatic soft actuator, such as a gripper, is feasible with this material.

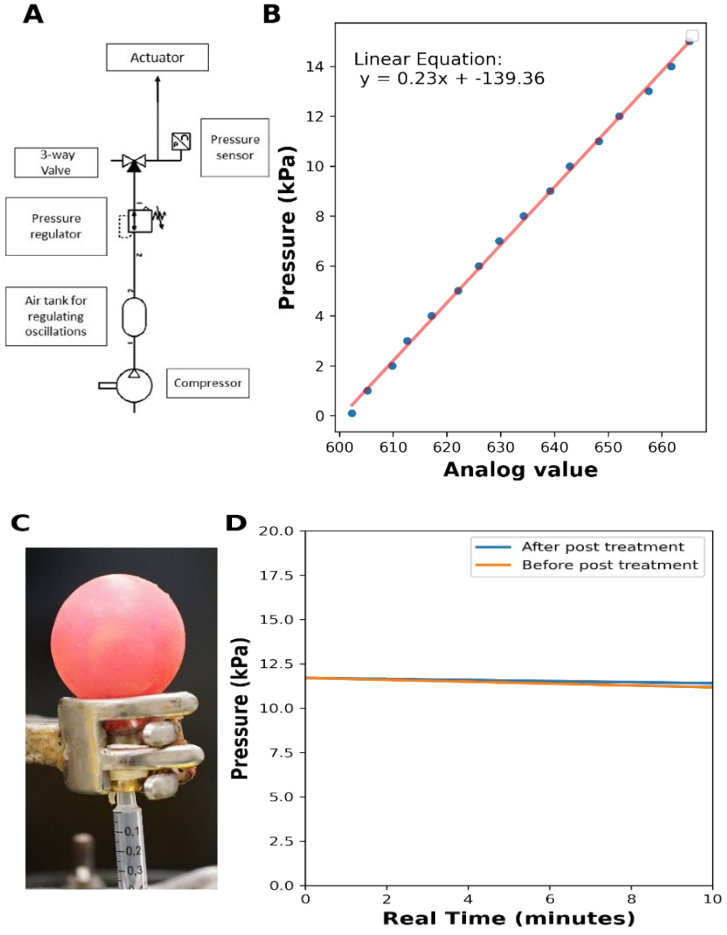

Supplementary Fig. S14: A.Schematic diagram of the pneumatic line designed for the air tightness test. B. Calibration curve of the pressure sensor, allowing for the extrapolation of the exact pressure within the working pressure range. C. 3D printed balloon made of the emulsion containing 35%wt water used for the air tightness test, with a pressure of 12 kPa imposed. D. Pressure-time graph showing the results of the air tightness test, where the pressure remained virtually unchanged for over 10 minutes after the valve's closure

Section 9: Analysis of the polymerized emulsion porosity behavior

We performed additional analysis using SEM measurement to examine the distribution of pores in the Z-axis at the surface and cross-sectional areas of the printed structure. As shown in Fig. S15 A-C, the behavior of pores on the surface is different compared to the cross-section, while the external surface is much less porous all around the structure and not only in a specific axis.

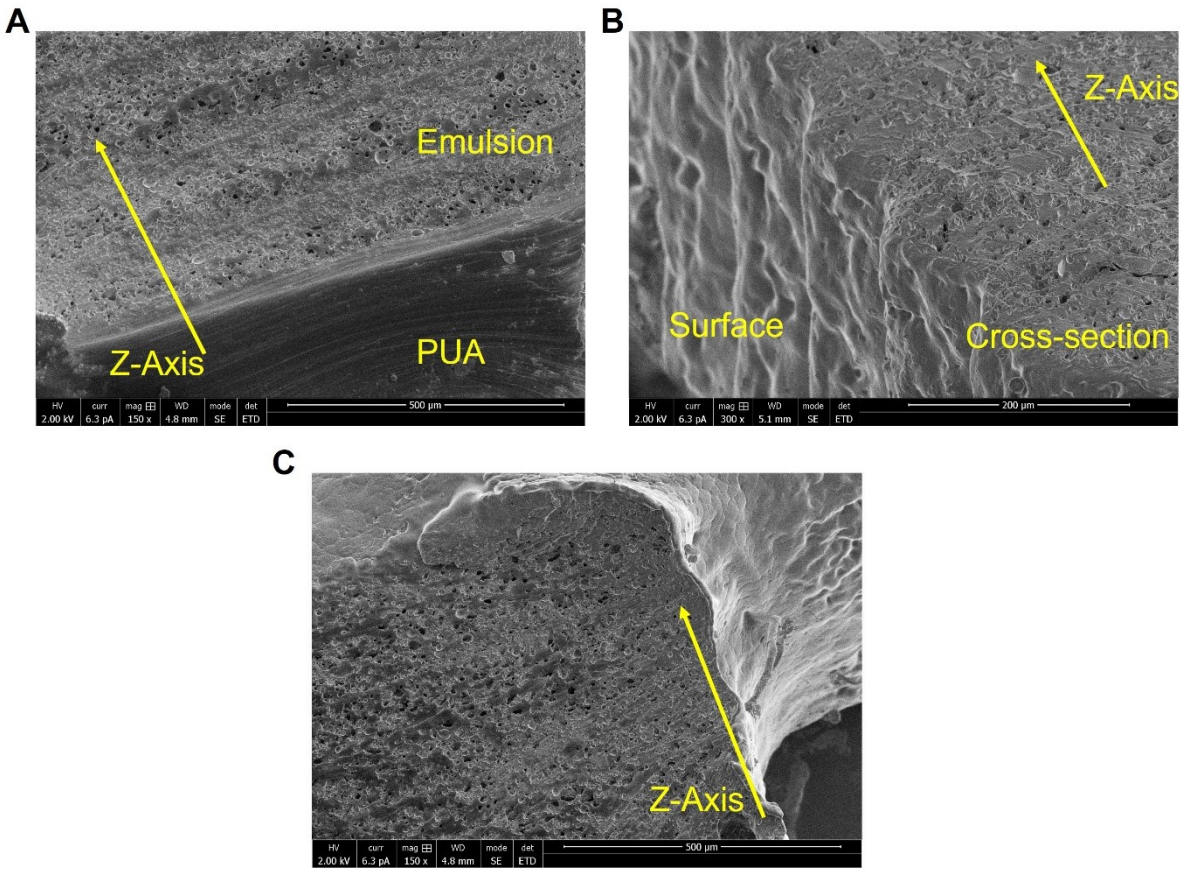

Supplementary Fig. S15: A-C. SEM image of polymerized emulsion with 35%wt water at the interface between the crosssection and the surface indication the Z axis direction.

To further show the overall porosity, we performed X-Ray micro-computed tomography (μCT) throughout the 3D structure. As shown in Fig. S16, the μCT scan have indeed detected an overall uniform porosity along the structure, however, it should be notes that the instrument resolution is limited to 4 μm, therefore the analysis was focused on the interconnectivity and overall porosity rather than the individual pores.

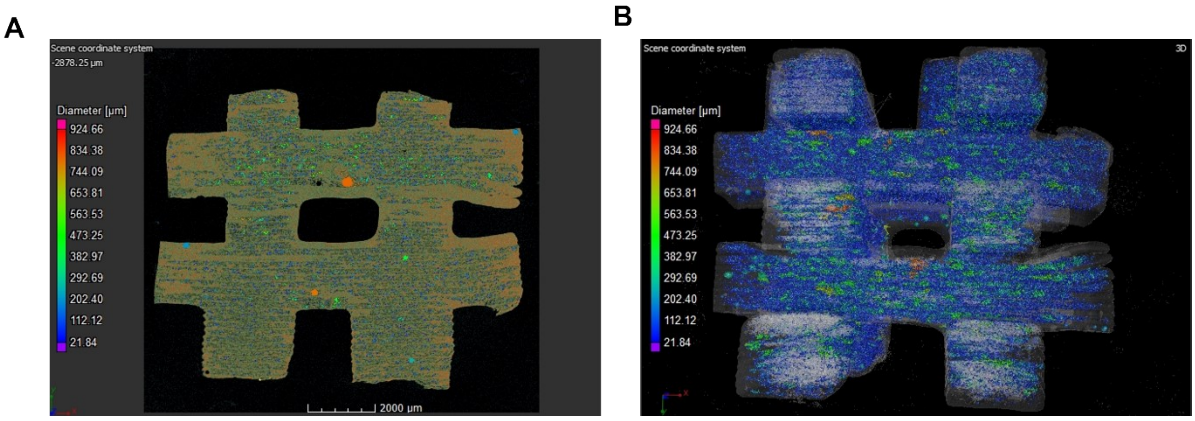

Supplementary Fig. S16: μCT scan of 3D printed emulsion showing the overall porosity and interconnectivity. A. 2D scan of cross section. B. 3D scan of all structure showing the porosity along the object.

Section 10: VLA evaluation FEM analysis and performance.
The parametric optimization is performed by means of a commercial FEM tool (ANSYS Inc., Canonsburg, PA, USA). Fig. S17A and B show isometric and side views of the VLA, respectively. Given the printing volume, the outer and inner radius of the VLA are fixed to 18 mm and 10 mm, respectively. The lattice layer has a 4 mm thickness and is composed of two 1 mm unit cells in radial direction (see Fig. S17C). The material properties of the VLA are definded by incompressible Neo-Hooken hyperelastic model (C10=197.265 kPa, Incompressible parameter D1=0). The best geometry of the VLA is identified by employing the parameterized model and static structure analysis.

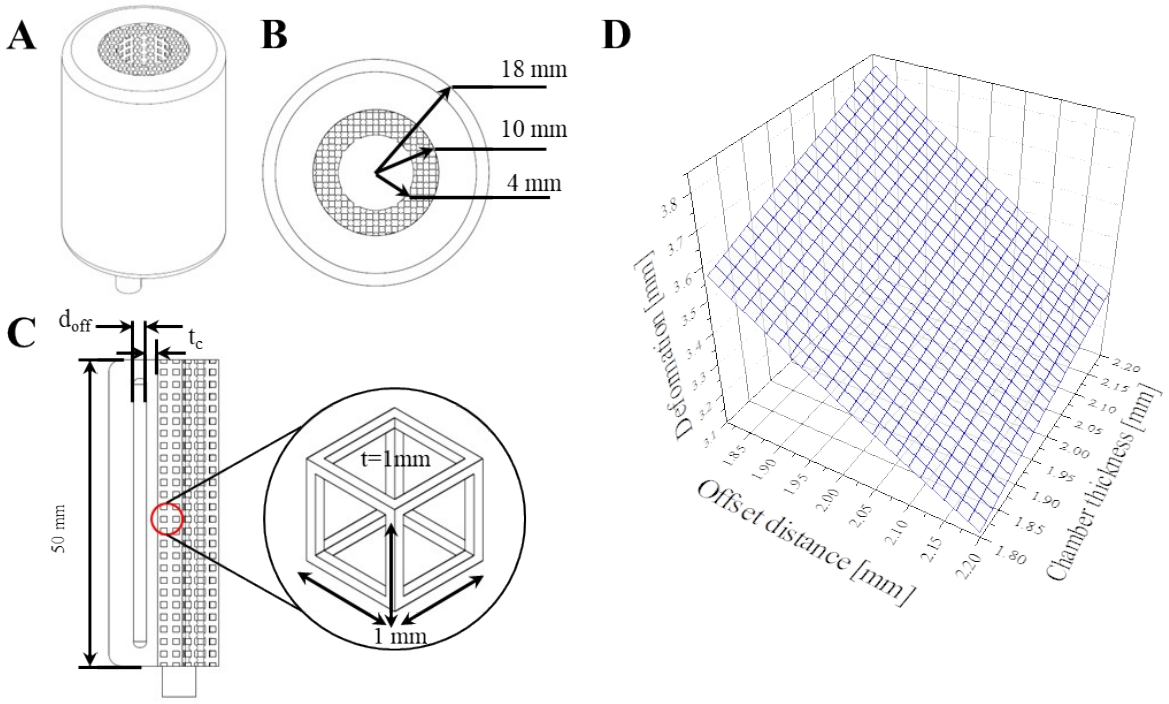

Supplementary Fig. S17: Optimization of the VAL design. A. Isometric view of the VLA B. Side view of the VLA: Outer diamter of 18 mm, inner diameter of 10 mm, and the elastic lattice layer of 4 mm thickness. C. Cross-section view of the VLA: the offeset distance (doff), the channel thickness (tc), the VLA length of 50 mm, and 1 mm unit cell with 1 mm thickness. D. Deformation response with respect to variation of the offset distance and of chamber thickness.

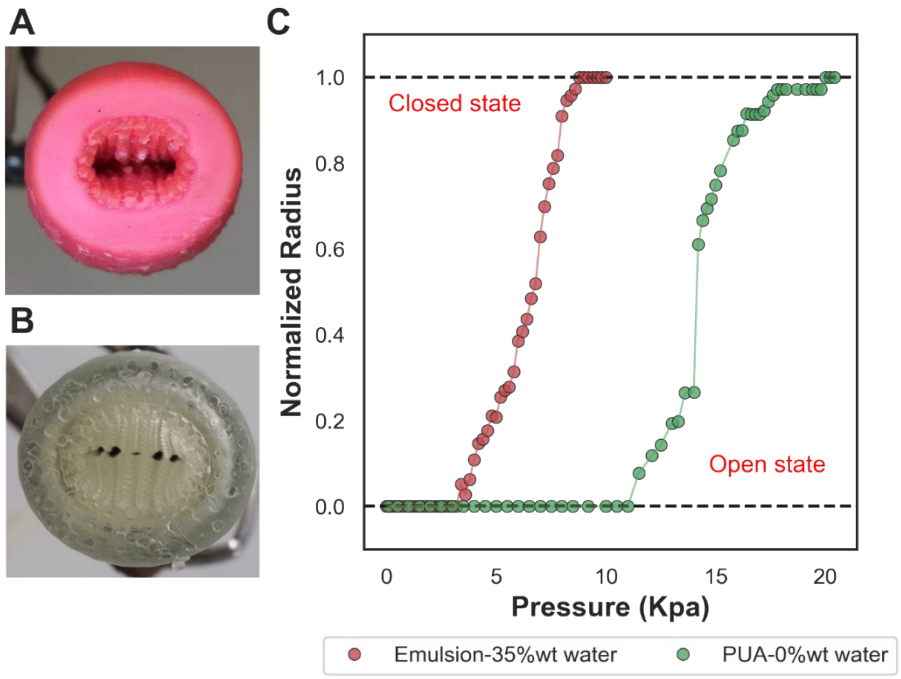

Supplementary Fig. S18: VLA performance comparison . A.photograph of VLA made of 35%wt water at its fully closed stated at 10 Kpas. B. photograph of VLA made of PUA only (0 %wt water) at its fully closed stated at 20.4 Kpas. C. Effect of pressure on the normelized radius of the VLA prepared with emulsion containing 35% water(Red) and PUA(Green)

References

1 I. Cooperstein, M. Layani and S. Magdassi, *J Mater Chem C Mater*, 2015, **3**, 2040–2044.

2 J. Choi, K. S. Hwang, Y. Kim, C. Lee, S. H. Ju, J. Kwon, W.-G. Koh and J.-Y. Lee, *Cite This: ACS Appl. Polym. Mater*, 2022, **2022**, 1570–1575.

3 A. Chiappone, A. Pedico, S. Porcu, C. F. Pirri, A. Lamberti and I. Roppolo, *Polymers (Basel)*, 2022, **14**, 5265.

4 Q. Wang, Ö. Karadas, O. Backman, L. Wang, T. Näreoja, J. M. Rosenholm, C. Xu and X. Wang, *Adv Healthc Mater*, 2023, 2203243.

5 M. Sušec, S. C. Ligon, J. Stampfl, R. Liska and P. Krajnc, *Macromol Rapid Commun*, 2013, **34**, 938–943.

6 N. S. Ozsoz, S. Pashneh-Tala and F. Claeyssens, *https://home.liebertpub.com/3dp*, , DOI:10.1089/3DP.2022.0235.

7 V. Hobiger, A.-L. Kutsch, J. Stampfl, R. Liska, S. Baudis and P. Krajnc, *https://home.liebertpub.com/3dp*, , DOI:10.1089/3DP.2022.0289.

8 J. R. Tumbleston, D. Shirvanyants, N. Ermoshkin, R. Janusziewicz, A. R. Johnson, D. Kelly, K. Chen, R. Pinschmidt, J. P. Rolland, A. Ermoshkin, E. T. Samulski and J. M. DeSimone, *Science (1979)*, 2015, **347**, 1349–1352.

9 J. Wu, J. Guo, C. Linghu, Y. Lu, J. Song, T. Xie and Q. Zhao, *Nature Communications 2021 12:1*, 2021, **12**, 1–9.

10 D. K. Patel, H. Sakhaei, M. Layani, B. Zhang, Q. Ge, S. Magdassi, D. K. Patel, S. Magdassi, A. H. Sakhaei, B. Zhang, Q. Ge and M. Layani, *Advanced Materials*, 2017, **29**, 1606000.